
Enhancing Perception Quality in Remote Sensing Image Compression via Invertible Neural Network

Junhui Li, Xingsong Hou*
Xi'an Jiaotong University

Abstract

Decoding remote sensing images to achieve high perceptual quality, particularly at low bitrates, remains a significant challenge. To address this problem, we propose the invertible neural network-based remote sensing image compression (INN-RSIC) method. Specifically, we capture compression distortion from an existing image compression algorithm and encode it as a set of Gaussian-distributed latent variables via INN. This ensures that the compression distortion in the decoded image becomes independent of the ground truth. Therefore, by leveraging the inverse mapping of INN, we can input the decoded image along with a set of randomly resampled Gaussian distributed variables into the inverse network, effectively generating enhanced images with better perception quality. To effectively learn compression distortion, channel expansion, Haar transformation, and invertible blocks are employed to construct the INN. Additionally, we introduce a quantization module (QM) to mitigate the impact of format conversion, thus enhancing the framework's generalization and improving the perceptual quality of enhanced images. Extensive experiments demonstrate that our INN-RSIC significantly outperforms the existing state-of-the-art traditional and deep learning-based image compression methods in terms of perception quality.

1 Introduction

Remote sensing (RS) images are widely used in many fields, including urban planning [1], biosphere monitoring [2], and land resource management [3]. However, RS images are typically characterized by high content, high resolution, and large size [4, 5]. Furthermore, with the advancement of sensor technology and the enhancement of the image acquisition capability of satellite and airborne equipment, the necessity of storing or transmitting RS images is also growing in importance. To cope with these challenges, high-resolution RS images are usually compressed before they are stored and transmitted to the ground. In this case, it is critical to achieve low-bitrate compression while obtaining the decoded images with high perceptual quality.

Traditional image compression standards, such as JPEG2000 [6], BPG [7], and VVC [8], have been instrumental in facilitating the storage and transmission of image data. However, image compression with these algorithms inevitably suffered from undesired blocking, ringing artifacts, and blurring [9, 10], which may highly influence the perception quality.

With the development of deep learning techniques, learning-based image compression methods have made significant progress in obtaining high rate-distortion performance [11, 12, 9, 13]. Notably, in natural image compression, Ballé et al. [14] introduced additional side information as a hyper-prior entropy model to estimate a zero-mean Gaussian distribution, laying the foundation for subsequent improvements in entropy modeling. Cheng et al. [10] further proposed the use of discretized Gaussian mixture likelihoods to parameterize the distributions of the entropy model,

*Correspondence to Xingsong Hou, houxs@mail.xjtu.edu.cn

resulting in impressive decoding performance. Meanwhile, He et al. [15] proposed an innovative uneven channel-conditional adaptive grouping scheme, enhancing compression performance without sacrificing computational speed. Despite the success of learning-based compression algorithms in natural scenes, RS images present unique challenges due to their rich texture, weak correlation, and low redundancy compared to natural images [16, 17]. Preserving visually pleasing decoded images while achieving high compression bitrates remains a significant challenge in RS image compression.

To tackle the challenge, Zhang et al. [11] introduced a multi-scale attention module to enhance the network’s feature extraction capability, and leveraged global priors and anchored-stripe attention to improve the entropy model. Pan et al. [18] employed generative adversarial networks (GANs) to independently decode the image content and detailed textures, subsequently fusing these features to achieve low-bitrate RS image compression. Additionally, Xiang et al. [19] utilized discrete wavelet transform to separate image features into high- and low-frequency components, and designed compression networks to enhance the model’s representation ability of both types of features.

In summary, the aforementioned deep learning-based image compression methods typically achieve image compression through CNN blocks [10, 15, 14, 13, 11, 19] or Transformer blocks [20–24], followed by optimization using distance measurements like L_1 , L_2 , or adversarial loss. Despite their impressive performance, these methods usually struggle to generate satisfactory perception quality. Recently, invertible neural network (INN) has emerged as a new paradigm for image generation, demonstrating remarkable performance across various applications [25–28]. Building on this success, several approaches have integrated INN into image compression to capture richer texture details [23, 26]. For instance, in [23], an enhanced INN-based encoding network was devised to improve the decoding performance of natural image compression. In [26], the authors utilized INN to develop an invertible image generation module, aiming to prevent information loss and propose a competitive low-bit-rate compression algorithm. In contrast to these methods, our approach focuses on leveraging the invertible capabilities of INN to recover more texture information of images decoded by an existing compression algorithm, without requiring additional bitstreams and model retraining. It is expected to sample some texture details from Gaussian distributed variables conditioned on the decoded image. Figure 1 illustrates the perception comparison between the decoded images and the enhanced images. It is observed that our INN-RSIC exhibits a high capability in recovering texture-rich details without additional bitrates.

In this paper, we propose an INN-based RS image compression (INN-RSIC) method. Specifically, we utilize an invertible forward network with conditional generation module (CGM) to encode compression loss information of an existing image compression algorithm into Gaussian-distributed latent variables. As a result, it is expected to sample some of the lost prior information from Gaussian distribution, thereby facilitating the recovery of visually enhanced images during the inverse mapping. Additionally, to effectively learn compression distortion, we adopt channel expansion and Haar transformation [29] to separate high and low frequency and introduce a quantization module (QM) to reduce the impact of the reconstruction quality due to data type conversion in the inference stage. The primary contributions of this paper can be summarized as follows: **1)** To the best of our knowledge, our INN-RSIC is the first attempt to model image compression distortion information of an existing image compression algorithm using invertible transforms. **2)** We develop a novel, effective yet simple architecture with channel expansion, Haar transform, and invertible blocks. This architecture enables projecting compression distortion into a case-agnostic distribution, so that compression distortion information can be obtained based on samples from a Gaussian distribution. **3)** CGM is introduced to split and encode the compression distortion information from ground truth into the latent variables conditioned on the synthetic image. This process generates pattern-free synthetic images and enhances the texture details of the reconstructed images during

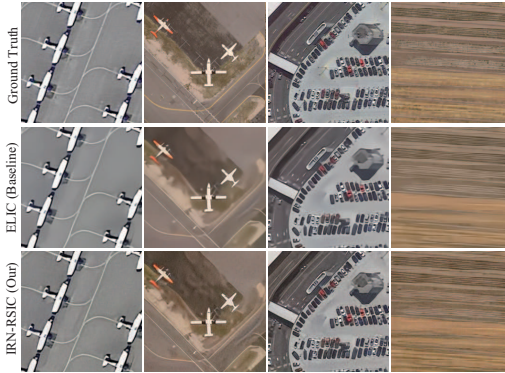


Figure 1: Visualization of the decoded results by ELIC [15] and our INN-RSIC.

the inverse mapping. 4) Extensive experiments indicate that our INN-RSIC outperforms the existing state-of-the-art traditional and learning-based image compression algorithms in terms of perceived quality, even at low bitrates. Our method offers a novel perspective for image compression algorithms to improve their quality-aware performance.

2 Related work

End-to-end RS image compression. In RS image compression, many researchers have directed their attention towards network structure and image transformation techniques. For instance, Pan et al. [18] adopted GANs to independently decode the image content and detailed textures, later combining these features to achieve low-bitrate compression of RS images. More recently, Xiang et al. [19] leveraged the discrete wavelet transform to separate image features into high- and low-frequency components. They then designed compression networks to bolster the model’s ability to present these features at different frequencies to recover texture-rich details.

Moreover, in the pursuit of advancing network modules for decoding more texture-rich details of RS image compression, some studies aim to improve the estimated accuracy of the entropy model. Pan et al. [9] proposed a hybrid attention network to improve the prediction accuracy of the entropy model and enhance the representation capabilities of both the encoder and decoder. In [4], a long-range convolutional network was developed as a network component to enhance the decoding performance of RS image compression. Fu et al. [30] considered the local and non-local redundancies presented in RS images and developed a mixed hyperprior network to explore both, thus improving the accuracy of entropy estimation. Besides, Zhang et al. [11] introduced a multi-scale attention module to enhance the network’s feature extraction capability, and employed global priors and anchored-stripe attention to improve the entropy model.

In summary, the above RS image compression algorithms mainly focus on designing complex networks for compact latent variable representation and more accurate entropy estimation to achieve texture-rich decoding results. Different from the above methods, we innovatively project the compression distortion loss of decoded images from an existing image compression algorithm into the Gaussian-distributed latent variables in the forward network, while combining the Gaussian distribution with the decoded images in the inverse network to obtain texture-rich enhanced images.

Invertible neural network (INN). INN offers several advantages, including bijective mapping, efficient mapping access, and computable Jacobi matrices, making them promising for various machine learning tasks [31–35]. For instance, Zhao et al. [25] employed INN to generate invertible grayscale images by separating color information from color images and encoding it into Gaussian-distributed latent variables. This approach ensures that the color information lost during grayscale generation remains independent of the input image. Similarly, Xiao et al. [36] developed invertible models to generate valid degraded images while transforming the distribution of lost contents to a fixed distribution of a latent variable during forward degradation. Restoration was then made tractable by applying the inverse transformation on the generated degraded image along with a randomly drawn latent variable. Liu et al. [33] considered image degradation and super-resolution as a pair of inverse tasks and replaced the generators in GAN with INN for unpaired image super-resolution. In addition, INN technology has been leveraged to improve the transformation between the image space and the latent feature space, thereby mitigating information loss [23]. For instance, Xie et al. [23] proposed an enhanced INN-based encoding network for better image compression. Gao et al. [26] integrated INN into the development of an invertible image generation module to prevent information loss and developed a competitive low-bitrate image compression algorithm.

3 The proposed INN-RSIC

RS images typically contain more detailed information compared to natural images, posing a greater challenge in obtaining texture-rich decoded RS images, especially at low bitrates [17]. Therefore, our INN-RSIC aims to utilize INN to encode the lost compression distortion of an existing image compression algorithm into a set of latent variables \mathbf{z} , following a pre-defined distribution, such as a Gaussian distribution. As a result, the distribution of latent variables becomes independent of the distribution of the input image. In the enhanced reconstruction stage of our framework (i.e., the inverse mapping of our INN-RSIC), a new set of randomly sampled latent variables $\bar{\mathbf{z}}$ can effectively

represent the lost compression distortion information to some extent. Thus, we can simply feed the re-sampled \tilde{z} , along with the decoded images, to the INN-RSIC of the inverse network for enhanced images.

Generally, the distribution of compression distortion information varies among different learning-based methods, as each exhibits distinct preferences in learning data distribution. For instance, some algorithms excel in achieving high performance on texture-rich images, while others have the opposite. Therefore, we focus here on the compression distortion distribution of the impressive image compression algorithm ELIC at different bitrates. Unfortunately, pinpointing the distortion distribution directly is challenging. Therefore, we choose to capture the distortion by investigating the relationship between the ground truth and the decoded image. In this way, we can indirectly explore the distortion distribution inherent in the compression algorithm.

Specifically, the framework of our INN-RSIC is depicted in Figure 2, consisting of a compressor and an enhancer. Given an input image \mathbf{x} , we utilize the competitive image compression algorithm ELIC [15] as the compressor to generate the decoded image $\tilde{\mathbf{x}}$, which serves as a label to constrain the generated synthetic image \mathbf{s} for training the enhancer. The enhancer mainly comprises two streams: the forward and inverse networks, denoted as $f_{\Theta}(\cdot)$ and $f_{\Theta}^{-1}(\cdot)$, respectively, where Θ represents the network parameters.

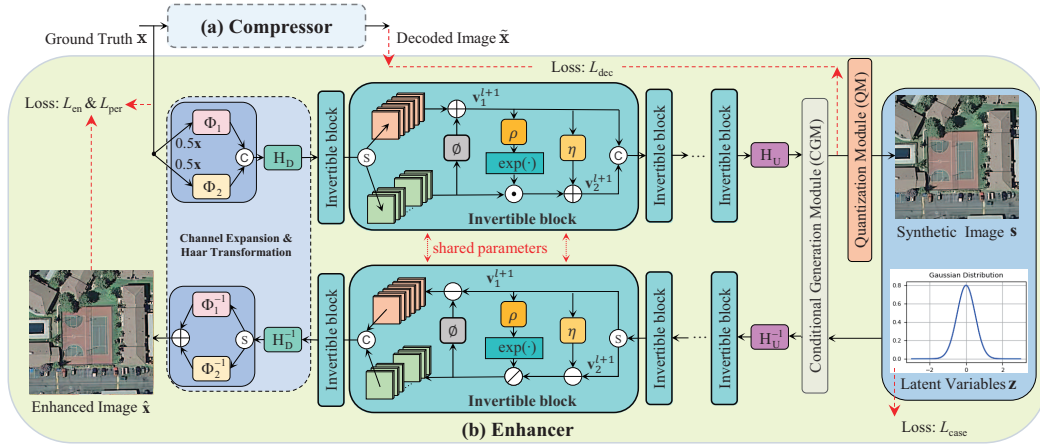


Figure 2: Illustration of our INN-RSIC. Compressor denotes the image compression algorithm [15].

3.1 INN architecture

3.1.1 Invertible block

The invertible block layer is a crucial component of invertible architectures, acting as a bridge to adapt between two different distributions via its trainable parameters. The structure of an invertible block is illustrated in Figure 2 (b). The inverse block operates on an input feature map $\mathbf{v} \in \mathbb{R}^{H \times W \times C}$, where H , W , and C denote height, width, and the number of channels, respectively. In each invertible block, \mathbf{v} is splitted along the channel dimension into two parts $[\mathbf{v}_1, \mathbf{v}_2]$, where $\mathbf{v}_1 \in \mathbb{R}^{H \times W \times C_1}$ and $\mathbf{v}_2 \in \mathbb{R}^{H \times W \times C_2}$, and $C_1 + C_2 = C$. To obtain the input features of the $(l+1)$ -th invertible block, inverse transformations are applied to both segments using learnable scale and shift parameters by

$$\mathbf{v}_1^{l+1} = \mathbf{v}_1^l + \phi(\mathbf{v}_2^l); \quad \mathbf{v}_2^{l+1} = \mathbf{v}_2^l \odot \exp(\rho(\mathbf{v}_1^{l+1})) + \eta(\mathbf{v}_1^{l+1}), \quad (1)$$

where \odot refers to Hadamard product. The $\phi(\cdot)$, $\rho(\cdot)$, and $\eta(\cdot)$ are realized by the dense block [37]. Thus, the inverse transformation can be derived from Eq. (1) by

$$\mathbf{v}_2^l = (\mathbf{v}_2^{l+1} - \eta(\mathbf{v}_1^{l+1})) \oslash \exp(\rho(\mathbf{v}_1^{l+1})); \quad \mathbf{v}_1^l = \mathbf{v}_1^{l+1} - \phi(\mathbf{v}_2^l), \quad (2)$$

where \oslash denotes element-wise division.

Besides, as illustrated in Figure 2 (b), the forward network outputs the synthetic image \mathbf{s} and the latent variable \mathbf{z} . Following the studies [26, 23], we assume that \mathbf{z} follows a Gaussian distribution,

which can be randomly sampled from the same distribution for the inverse mapping. Consequently, in the training stage, the synthetic image \mathbf{s} and \mathbf{z} can be merged and fed into the inverse network for model optimization. In the inference stage, the decoded image $\tilde{\mathbf{x}}$ and resampled $\tilde{\mathbf{z}} \sim \mathcal{N}(0, \mathbf{I})$ can be combined and fed into the inverse network for image enhancement.

3.1.2 Channel expansion and Haar transformation

Within each invertible block, the channels of both its input and output signals have the same number. However, in addition to generating the synthetic image, we also need to produce an expanded output to derive the Gaussian latent variable \mathbf{z} . To achieve this, as shown in Figure 2 (b), we double the number of channels of the input image by using 1×1 convolutional layers. In addition, Haar transformation [29] is used here to separate the compression distortion information by splitting the high and low frequencies, which are then fed into the invertible blocks.

Specifically, in the forward network, given the ground truth \mathbf{x} , the feature \mathbf{F} fed into the first invertible block can be expressed as

$$\mathbf{F} = H_D(\text{Concat}(\Phi_1(\mathbf{x}/2.0), \Phi_2(\mathbf{x}/2.0))), \quad (3)$$

where $H_D(\cdot)$ denotes Haar function, and $\text{Concat}(\cdot)$ refers to a concatenation operation. $\Phi_1(\cdot)$ and $\Phi_2(\cdot)$ refer to two 1×1 convolution layers. After the last invertible block, the inverse Haar function $H_U(\cdot)$ is adopted to transform the features from the frequency domain to the spatial domain.

As a result, at the end of the forward network, we can thus obtain six-channel signals with the same size as the input image, and with CGM, we derive both the synthetic image Θ and Gaussian latent variables \mathbf{z} , which are then combined and fed into the inverse network for image recovery.

In the inverse network, the inverse processing of Eq. (3) can be formulated as

$$\mathbf{p}_i = \text{Split}(H_D^{-1}(\mathbf{F})), \quad i \in \{1, 2\}; \quad \mathbf{x} = \Phi_1^{-1}(\mathbf{p}_1) + \Phi_2^{-1}(\mathbf{p}_2), \quad (4)$$

where $\Phi_1^{-1}(\cdot)$, $\Phi_2^{-1}(\cdot)$, and $H_D^{-1}(\cdot)$ refer to the inverse functions of $\Phi_1(\cdot)$, $\Phi_2(\cdot)$, and $H_D(\cdot)$, respectively. Next, we will illustrate CGM in detail.

3.1.3 Conditional generation module (CGM)

As illustrated above, we aim to encode the compression distortion information of decoded RS images into a set of Gaussian-distributed latent variables, where the mean and variance are conditioned on the synthetic image. This conditioning enables the reconstruction process to be image-adaptive. To achieve this, as illustrated in Figure 2 (b), we introduce a CGM at the end of the forward network. Specifically, to establish the dependency between \mathbf{s} and \mathbf{z} , as depicted in Figure 3, the output six-channel tensor \mathbf{g} from the last invertible block is further divided by CGM into two parts: a three-channel synthetic image \mathbf{s} and a three-channel latent variable $\tilde{\mathbf{z}}$ representing the compression distortion information.

In the forward mapping, inspired by [25], we normalize $\tilde{\mathbf{z}}$ into standard Gaussian-distributed variables \mathbf{z} by $\mathbf{z} = (\tilde{\mathbf{z}} - \boldsymbol{\mu}) \oslash \boldsymbol{\sigma}$, where $\mathbf{z} \sim \mathcal{N}(0, \mathbf{I})$, where the mean and scale of \mathbf{s} can be calculated by

$$\boldsymbol{\mu} = \psi_1(\mathbf{s}); \quad \boldsymbol{\sigma} = \exp(\psi_2(\mathbf{s})), \quad (5)$$

where $\psi_1(\cdot)$ and $\psi_2(\cdot)$ are achieved by the dense block [37]. Hence, its reverse mapping can be formulated as $\tilde{\mathbf{z}} = \mathbf{z} \odot \boldsymbol{\sigma} + \boldsymbol{\mu}$, where $\tilde{\mathbf{z}} \sim \mathcal{N}(\boldsymbol{\mu}, \boldsymbol{\sigma})$. In this way, we encode the compression distortion information into the latent variables, whose distribution is conditioned on the synthetic image. The inverse network is similar to [36, 25], where we sample a set of random variables from Gaussian distribution conditioned on the synthetic images to reconstruct the enhanced images.

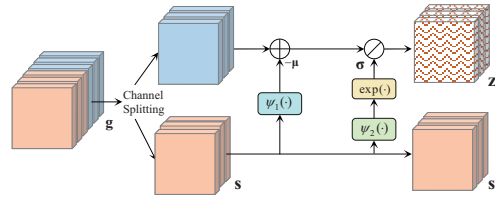


Figure 3: Illustration of the conditional generation module (CGM).

3.1.4 Quantization module (QM)

To ensure compatibility with common decoded image storage formats such as RGB (8 bits for each R, G, and B color channels), as shown in Figure 2 (b), we integrate QM after CGM. This module

converts the floating-point values of the produced synthetic images into 8-bit unsigned integers by a rounding operation for quantization. However, it’s essential to acknowledge a significant obstacle: the quantization module is inherently non-differentiable. To address this challenge, we use the Straight-Through Estimator technique as employed in [15] to ensure that INN-RSIC is effectively optimized during the training process. Subsequently, in the inference stage, the decoded image can be reasonably fed into the inverse network for image enhancement.

3.2 Optimization strategy

3.2.1 Compression optimization loss

As we aim to capture the compression distortion of ELIC [15], here we provide a brief overview of its loss function. Specifically, to balance the compression ratio and the image quality of the decoded image of ELIC, the loss function is defined as

$$\mathcal{L}_1 = R + \lambda D(\mathbf{x}, \tilde{\mathbf{x}}), \quad (6)$$

where the rate R refers to the entropy of the quantized latent variables of ELIC. Meanwhile, $D(\cdot, \cdot)$ denotes the similarity between the input image and the decoded image, typically measured by using mean squared error (MSE). Different compression rates can be achieved by adjusting the hyperparameter λ , where the higher the value of λ , the higher the bits per pixel (bpp) and the better the image quality.

3.2.2 Forward presentation loss

The forward network is primarily focused on enabling the proposed model to capture the compression distortion distribution of the decoded image. This is achieved by establishing a correspondence between the input image \mathbf{x} and the decoded image $\tilde{\mathbf{x}}$, as well as a case-agnostic distribution $p(\mathbf{z})$ of \mathbf{z} . It can be realized by developing two loss functions: decoded image loss and case-agnostic distribution loss.

Decoded image loss. To generate the guidance images for training the forward network, ELIC is adopted to generate the labeled image $\tilde{\mathbf{x}}$, which can be formulated as

$$\tilde{\mathbf{x}} = \text{ELIC}(\mathbf{x}, \lambda). \quad (7)$$

Thereafter, to make our model follow the guidance, we drive the synthetic image $\mathbf{s} = f_{\Theta}(\mathbf{x})$ to resemble $\tilde{\mathbf{x}}$, which can be derived by

$$L_{\text{dec}} = \|f_{\Theta}(\mathbf{x}) - \tilde{\mathbf{x}}\|^2. \quad (8)$$

Case-agnostic distribution loss. To regularize the distribution of \mathbf{z} , we maximize the log-likelihood of $p(\mathbf{z})$, inspired by [25]. Thus, the loss function to constrain the latent variables \mathbf{z} can be formulated as

$$L_{\text{case}} = -\log(p(\mathbf{z})) = -\log\left(\frac{1}{(2\pi)^{M/2}} \exp\left(-\frac{1}{2}\|\mathbf{z}\|^2\right)\right), \quad (9)$$

where M is the dimensionality of \mathbf{z} . This constraint penalizes the normalized latent variables \mathbf{z} to follow standard Gaussian distribution. Consequently, in the inverse reconstruction processing, we can randomly sample a set of Gaussian-distributed variables along with the synthetic image to obtain the reconstructed image.

3.2.3 Reverse reconstruction loss

The inverse network aims to guide the model in recovering visually appealing images using randomly sampled latent variables and synthetic images. This is achieved by developing two loss functions: enhancement reconstruction loss and quality perception loss.

Enhancing reconstruction loss. In theory, the synthetic image can be perfectly restored to the corresponding ground truth version through the inverse network of INN because there is no information omission. However, in practice, the decoded image is not generated by the forward network of our INN-RSIC but with an image compression method. That is, the synthetic image should be stored in 8-bit unsigned integer format so that the decoded image can be used directly instead of the synthetic

image here for image detail enhancement during the inference stage. To address this, we adopt QM at the end of the forward network during training. Consequently, by penalizing the discrepancy between the reconstructed image and the ground truth, we can derive the enhancing reconstruction loss given as

$$L_{\text{en}} = \|f_{\Theta}^{-1}(\mathbf{s}, \vec{\mathbf{z}}) - \mathbf{x}\|^2, \quad (10)$$

where $\vec{\mathbf{z}}$ denotes the re-sampled latent variables from standard Gaussian distribution, and the synthetic image can be derived by $\mathbf{s} = \text{QM}(f_{\Theta}(\mathbf{x}))$.

Quality perception loss. To improve the perceptual performance of the network by estimating distances in predefined feature space rather than image space, a perceptual loss function called L_{per} is used here. In other words, the feature space distance is represented by an optimization function, which serves as a driver for the network to perform image reconstruction while retaining a feature representation similar to the ground truth. Concretely, the learning perceptual image patch similarity (LPIPS) [38] is utilized to indicate the perceptual loss, which is defined as

$$L_{\text{per}} = \|\text{Vgg}(\hat{\mathbf{x}}) - \text{Vgg}(\mathbf{x})\|^2, \quad (11)$$

where $\text{Vgg}(\cdot)$ denotes a feature function that leverages the features extracted at the "Conv4-4" layer of VGG19 to penalize the contrast similarity between $\hat{\mathbf{x}}$ and \mathbf{x} , as adopted in [39].

Therefore, the total loss function can be given by

$$L_{\text{total}} = \lambda_1 L_{\text{dec}} + \lambda_2 L_{\text{case}} + \lambda_3 L_{\text{en}} + \lambda_4 L_{\text{per}}, \quad (12)$$

where $\lambda_1, \lambda_2, \lambda_3$, and λ_4 are hyperparameters used to balance the different loss terms.

Thus, after obtaining the trained model, in the inference stage, given a decoded image $\tilde{\mathbf{x}}$ by using Eq. (7), we can derive its enhanced image $\hat{\mathbf{x}}$ by $\hat{\mathbf{x}} = f_{\Theta}^{-1}(\tilde{\mathbf{x}}, \vec{\mathbf{z}})$, where $\vec{\mathbf{z}}$ refers to the latent variables sampled from Gaussian distribution $\vec{\mathbf{z}} \sim \mathcal{N}(0, \mathbf{I})$. It can be observed that there is no additional bitrates acquirement for the enhancement processing of the decoded image.

4 Experiments

4.1 Experimental Settings

Datasets. To evaluate the effectiveness of our INN-RSIC, we conducted experiments using two datasets: DOTA [40] and UC-Merced (UC-M) [41], as adopted in [18, 9]. In our experiment, the training dataset of DOTA and 80% of the UC-M training set are used for model training. During training, the images in the training dataset are randomly cropped into 128×128 resolution, and several augmentation strategies, such as random horizontal flip, random vertical flip, and random crop, are adopted. To evaluate the performance of the proposed model, we randomly selected 100 images from the DOTA testing dataset, further cropped each image to a resolution of 256×256 , and selected 10% images from UC-M as the testing set.

Implementation details. In this experiment, ELIC [15] is employed to compress the images of the training dataset. Specifically, five models are trained with parameters $\lambda \in \{4, 8, 32, 100, 450\} \times 10^{-4}$, and these models are used to separately generate the decoded images, which are then utilized as labeled images to constrain the forward latent representation. As different compression levels correspond to various compression distortion distributions of ELIC, the labeled images under each λ are used to train an INN-RSIC model. Besides, to train the proposed model, the widely-used AdamW [42] with $\beta_1 = 0.9$ and $\beta_2 = 0.999$ is employed for parameter optimization. The hyperparameters $\lambda_1, \lambda_2, \lambda_3$, and λ_4 are experimentally set to 1.0, 200.0, 0.05, and 0.01, respectively. The initial learning rate α is set to $1e-4$ and the total number of epochs is set to 300, with the learning rate halved every 60 epochs until it reaches a value smaller than $1e-6$. PSNR, MS-SSIM, FID [43], and LPIPS are employed as the evaluation metrics.

4.2 Performance evaluation

In this section, we conduct a comprehensive comparison between our INN-RSIC and various traditional and learning-based image compression algorithms, using the testing set of DOTA and UC-M. The benchmark includes the state-of-the-art image compression algorithms, including traditional

standards such as JPEG2000 [6], BPG [7], VVC (YUV4:4:4) [8], as well as the competitive learning-based image compression algorithms like Entroformer [21], STF [20], and ELIC [15].

The FID and LIPIS comparisons of these algorithms on the testing set of DOTA and UC-M are shown in Figure 4. It can be observed that our INN-RSIC outperforms all other methods in terms of FID and LIPIS, including traditional and deep learning-based methods, on both datasets. Furthermore, we note that at very low bpp, the improvement in both FID and LIPIS is small, which may be because the distortion of the decoded image is too high for our INN-RSIC to stably recover more details from the Gaussian distribution, which is conditioned on the decoded image. As the bpp increases, our INN-RSIC exhibits significantly superior performance in terms of FID and LIPIS.

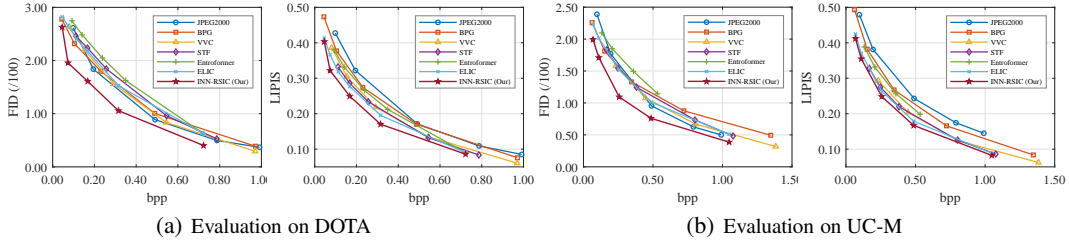


Figure 4: Performance comparison of several image compression algorithms on the testing set of DOTA and UC-M in terms of FID and LIPIS.

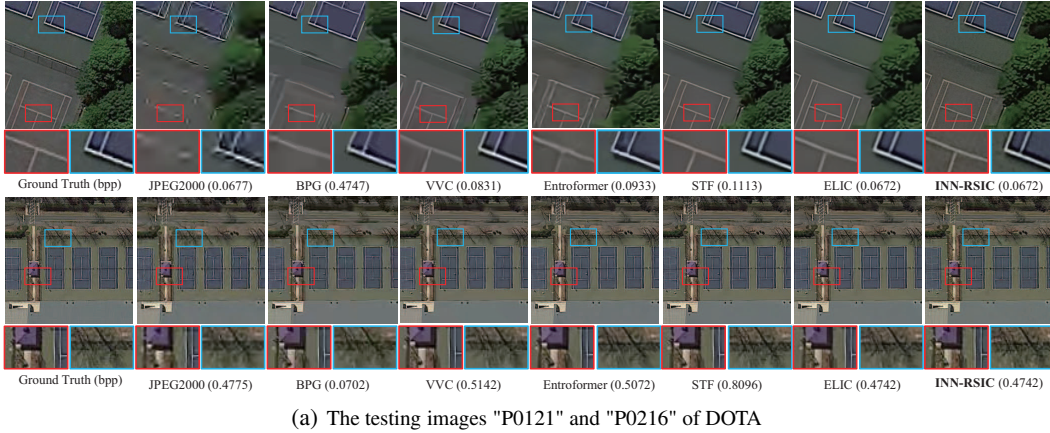


Figure 5: Visualization of the decoding performance on the testing images of DOTA and UC-M.

Besides, Figure 5 shows the decoding results of these algorithms on the testing images of DOTA and UC-M at low and high bitrates. In Figure 5 (a), it's noticeable that the image "P0121" decoded by

the state-of-the-art traditional compression algorithm VVC exhibits obvious distortion, even with an additional 23.66% increase of bpp compared to our INN-RSIC. Moreover, the decoded image from the competitive learning-based compression algorithm STF still suffers from significant distortion, despite a 70.73% increase of bpp. At high bitrates, the decoded image "P0216" by VVC presents blurry texture details despite the higher bpp. Particularly, it is evident that the image perception quality of the decoded image by STF remains inferior to that of our INN-RSIC, even with a 65.63% increase in additional bpp. Similarly, as depicted in Figure 5 (b), the results further indicate that our INN-RSIC demonstrates impressive perception quality compared to traditional and deep learning-based image compression algorithms at both low and high bitrates.

In summary, we can safely demonstrate that our INN-RSIC effectively and impressively contributes to the detailed recovery of decoded images without increasing additional bitrates.

4.3 Ablation studies

Effectiveness of QM. The QM considers the impact of format mismatch on the reconstruction performance of the inverse mapping. Table 1 reports the quality metrics of the proposed model with and without QM for enhancing the decoded images of ELIC on the testing set of DOTA and UC-M. From the results, it can be seen that the proposed model with QM presents better perception quality results with comparable PSNR and MS-SSIM metrics on both datasets. The reason lies in the fact that the input images fed into our INN-RSIC are 3-channel 8-bit RGB images during the inference stage, and QM can better contribute to the proposed model to match the data type of the input images. Moreover, the lower PSNR and MS-SSIM values of the enhanced images originate from the inherent reversibility of INN. Since the ground truth is not available at the decoding end, i.e., the synthetic image is not available, we therefore use the decoded image as the inverse input to our INN-RSIC in the inference stage.

Effectiveness of CGM. The CGM aims to incorporate guidance from synthetic images into the latent variables during the reconstruction of texture-rich images. To demonstrate the effectiveness of this approach, Table 1 presents the performance of our INN-RSIC with and without CGM on the testing sets of DOTA and UC-M. It is evident that the INN-RSIC with CGM consistently outperforms the model without CGM in terms of FID and LIPIS. This implies that encoding latent variables into Gaussian distributed variables conditioned on synthetic images can enhance the reconstruction performance during inverse mapping. This observation is consistent with the earlier study in [25].

Table 1: Quantitative comparison of our INN-RSIC with and without (w/o) QM or CGM.

Datasets	Methods	PSNR \uparrow	MS-SSIM \uparrow	FID \downarrow	LIPIS \downarrow
DOTA	w/o QM	28.11	0.8955	236.8280	0.3521
	w/o CGM	28.00	0.8949	235.6634	0.3496
	INN-RSIC	27.57	0.8871	195.6175	0.3218
UC-M	w/o QM	26.09	0.9061	174.5280	0.3600
	w/o CGM	26.05	0.9055	173.9155	0.3556
	INN-RSIC	26.00	0.9053	170.9994	0.3547

5 Conclusion

In this paper, we introduce INN-RSIC, a method aims at enhancing the perceptual quality of decoded RS images. This approach encodes the compression distortion from an image compression algorithm into Gaussian-distributed latent variables and recovers from the perspective of invertible transformation to substantially restore more texture details. Additionally, a CGM is introduced to split and encode the compression distortion information from the ground truth into latent variables conditioned on the synthetic image, thus improving the reconstruction of the enhanced image. Moreover, a QM is introduced to weaken the impact of data type conversions on reconstruction quality during the inference stage. Extensive experiments conducted on two widely used RS image datasets demonstrate that our INN-RSIC significantly outperforms existing traditional and learning-based image compression algorithms in terms of perception quality. Furthermore, our approach presents a new perspective for RS image compression algorithms to enhance texture reconstruction capabilities, particularly by minimizing the gap between synthetic and decoded images.

References

- [1] Z. Xie, M. Yuan, F. Zhang, M. Chen, J. Shan, L. Sun, and X. Liu, "Using remote sensing data and graph theory to identify polycentric urban structure," *IEEE Geoscience and Remote Sensing Letters*, vol. 20, pp. 1–5, 2023.
- [2] Z. Zhang, W. Xu, Z. Shi, and Q. Qin, "Establishment of a comprehensive drought monitoring index based on multisource remote sensing data and agricultural drought monitoring," *IEEE Journal of Selected Topics in Applied Earth Observations and Remote Sensing*, vol. 14, pp. 2113–2126, 2021.
- [3] Z. Lv, H. Huang, W. Sun, T. Lei, J. A. Benediktsson, and J. Li, "Novel enhanced unet for change detection using multimodal remote sensing image," *IEEE Geoscience and Remote Sensing Letters*, vol. 20, pp. 1–5, 2023.
- [4] S. Xiang and Q. Liang, "Remote sensing image compression with long-range convolution and improved non-local attention model," *Signal Processing*, vol. 209, p. 109005, 2023.
- [5] Y. Li, J. Ma, and Y. Zhang, "Image retrieval from remote sensing big data: A survey," *Information Fusion*, vol. 67, pp. 94–115, 2021.
- [6] D. S. Taubman, M. W. Marcellin, and M. Rabbani, "JPEG2000: Image compression fundamentals, standards and practice," *Journal of Electronic Imaging*, vol. 11, no. 2, pp. 286–287, 2002.
- [7] F. Bellard, "BPG image format." [Online]. Available: <https://bellard.org/bpg>.
- [8] "Versatile video coding reference software version 16.0 (vtm-16.0)." [Online]. Available: <https://vcgit.hhi.fraunhofer.de/jvet/VVCSsoftware-VTM/-/releases/VTM-16.0>.
- [9] T. Pan, L. Zhang, Y. Song, and Y. Liu, "Hybrid attention compression network with light graph attention module for remote sensing images," *IEEE Geoscience and Remote Sensing Letters*, vol. 20, pp. 1–5, 2023.
- [10] Z. Cheng, H. Sun, M. Takeuchi, and J. Katto, "Learned image compression with discretized Gaussian mixture likelihoods and attention modules," in *IEEE Conference on Computer Vision and Pattern Recognition (CVPR)*, 2020, pp. 7939–7948.
- [11] L. Zhang, X. Hu, T. Pan, and L. Zhang, "Global priors with anchored-stripe attention and multiscale convolution for remote sensing image compression," *IEEE Journal of Selected Topics in Applied Earth Observations and Remote Sensing*, vol. 17, pp. 138–149, 2024.
- [12] F. Mentzer, G. D. Toderici, M. Tschannen, and E. Agustsson, "High-fidelity generative image compression," in *Advances in Neural Information Processing Systems (NIPS)*, vol. 33. Curran Associates, Inc., 2020, pp. 11 913–11 924.
- [13] Z. Tang, H. Wang, X. Yi, Y. Zhang, S. Kwong, and C.-C. J. Kuo, "Joint graph attention and asymmetric convolutional neural network for deep image compression," *IEEE Transactions on Circuits and Systems for Video Technology*, vol. 33, no. 1, pp. 421–433, 2022.
- [14] J. Ballé, D. Minnen, S. Singh, S. J. Hwang, and N. Johnston, "Variational image compression with a scale hyperprior," in *International Conference on Learning Representations (ICLR)*, 2018.
- [15] D. He, Z. Yang, W. Peng, R. Ma, H. Qin, and Y. Wang, "Elic: Efficient learned image compression with unevenly grouped space-channel contextual adaptive coding," in *IEEE Conference on Computer Vision and Pattern Recognition (CVPR)*, 2022, pp. 5718–5727.
- [16] X. Lu, B. Wang, X. Zheng, and X. Li, "Exploring models and data for remote sensing image caption generation," *IEEE Transactions on Geoscience and Remote Sensing*, vol. 56, no. 4, pp. 2183–2195, 2017.
- [17] P. Han, B. Zhao, and X. Li, "Edge-guided remote-sensing image compression," *IEEE Transactions on Geoscience and Remote Sensing*, vol. 61, pp. 1–15, 2023.

- [18] T. Pan, L. Zhang, L. Qu, and Y. Liu, “A coupled compression generation network for remote-sensing images at extremely low bitrates,” *IEEE Transactions on Geoscience and Remote Sensing*, vol. 61, pp. 1–14, 2023.
- [19] S. Xiang and Q. Liang, “Remote sensing image compression based on high-frequency and low-frequency components,” *IEEE Transactions on Geoscience and Remote Sensing*, vol. 62, pp. 1–15, 2024.
- [20] R. Zou, C. Song, and Z. Zhang, “The devil is in the details: Window-based attention for image compression,” in *IEEE Conference on Computer Vision and Pattern Recognition (CVPR)*, 2022, pp. 17 492–17 501.
- [21] Y. Qian, X. Sun, M. Lin, Z. Tan, and R. Jin, “Entroformer: A transformer-based entropy model for learned image compression,” in *International Conference on Learning Representations (ICLR)*, 2022.
- [22] S. Xiang, Q. Liang, and L. Fang, “Discrete wavelet transform-based gaussian mixture model for remote sensing image compression,” *IEEE Transactions on Geoscience and Remote Sensing*, vol. 61, pp. 1–12, 2023.
- [23] Y. Xie, K. L. Cheng, and Q. Chen, “Enhanced invertible encoding for learned image compression,” in *Proceedings of the 29th ACM international conference on multimedia*, 2021, pp. 162–170.
- [24] J. Li and X. Hou, “Object-fidelity remote sensing image compression with content-weighted bitrate allocation and patch-based local attention,” *IEEE Transactions on Geoscience and Remote Sensing*, pp. 1–1, 2024.
- [25] R. Zhao, T. Liu, J. Xiao, D. P. K. Lun, and K.-M. Lam, “Invertible image decolorization,” *IEEE Transactions on Image Processing*, vol. 30, pp. 6081–6095, 2021.
- [26] F. Gao, X. Deng, J. Jing, X. Zou, and M. Xu, “Extremely low bit-rate image compression via invertible image generation,” *IEEE Transactions on Circuits and Systems for Video Technology*, pp. 1–1, 2023.
- [27] S. T. Radev, U. K. Mertens, A. Voss, L. Ardizzone, and U. Köthe, “Bayesflow: Learning complex stochastic models with invertible neural networks,” *IEEE Transactions on Neural Networks and Learning Systems*, vol. 33, no. 4, pp. 1452–1466, 2022.
- [28] M. Zhou, X. Fu, J. Huang, F. Zhao, A. Liu, and R. Wang, “Effective pan-sharpening with transformer and invertible neural network,” *IEEE Transactions on Geoscience and Remote Sensing*, vol. 60, pp. 1–15, 2022.
- [29] A. Haar, *Zur theorie der orthogonalen funktionensysteme*. Georg-August-Universität, Göttingen., 1909.
- [30] C. Fu and B. Du, “Remote sensing image compression based on the multiple prior information,” *Remote Sensing*, vol. 15, no. 8, 2023.
- [31] R. Rombach, P. Esser, and B. Ommer, “Network-to-network translation with conditional invertible neural networks,” in *Advances in Neural Information Processing Systems (NIPS)*, vol. 33. Curran Associates, Inc., 2020, pp. 2784–2797.
- [32] J.-J. Huang and P. L. Dragotti, “Winnet: Wavelet-inspired invertible network for image denoising,” *IEEE Transactions on Image Processing*, vol. 31, pp. 4377–4392, 2022.
- [33] H. Liu, M. Shao, Y. Qiao, Y. Wan, and D. Meng, “Unpaired image super-resolution using a lightweight invertible neural network,” *Pattern Recognition*, vol. 144, p. 109822, 2023.
- [34] M. Zhou, J. Huang, X. Fu, F. Zhao, and D. Hong, “Effective pan-sharpening by multiscale invertible neural network and heterogeneous task distilling,” *IEEE Transactions on Geoscience and Remote Sensing*, vol. 60, pp. 1–14, 2022.

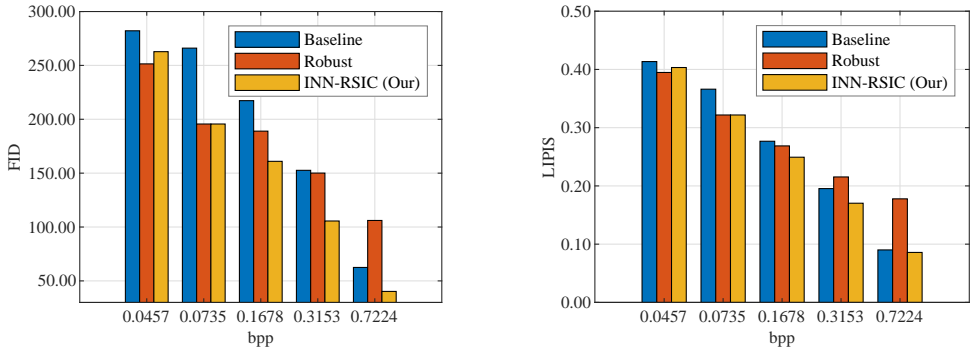
- [35] Y. Song, C. Meng, and S. Ermon, “Mintnet: Building invertible neural networks with masked convolutions,” in *Advances in Neural Information Processing Systems (NIPS)*, vol. 32. Curran Associates, Inc., 2019.
- [36] M. Xiao, S. Zheng, C. Liu, Y. Wang, D. He, G. Ke, J. Bian, Z. Lin, and T.-Y. Liu, “Invertible image rescaling,” in *Computer Vision – ECCV 2020*. Cham: Springer International Publishing, 2020, pp. 126–144.
- [37] X. Wang, K. Yu, S. Wu, J. Gu, Y. Liu, C. Dong, Y. Qiao, and C. Change Loy, “Esrgan: Enhanced super-resolution generative adversarial networks,” in *Proceedings of the European Conference on Computer Vision (ECCV) Workshops*, 2018, pp. 0–0.
- [38] R. Zhang, P. Isola, A. A. Efros, E. Shechtman, and O. Wang, “The unreasonable effectiveness of deep features as a perceptual metric,” in *IEEE Conference on Computer Vision and Pattern Recognition (CVPR)*, 2018, pp. 586–595.
- [39] M. Xia, X. Liu, and T.-T. Wong, “Invertible grayscale,” *ACM Transactions on Graphics*, vol. 37, no. 6, dec 2018.
- [40] Y. L. G.-S. X. Q. L. Jian Ding, Nan Xue, “Learning roi transformer for detecting oriented objects in aerial images,” in *IEEE Conference on Computer Vision and Pattern Recognition (CVPR)*, June 2019.
- [41] Y. Yang and S. Newsam, “Bag-of-visual-words and spatial extensions for land-use classification,” in *Proceedings of the 18th SIGSPATIAL International Conference on Advances in Geographic Information Systems*, 2010, pp. 270–279.
- [42] I. Loshchilov and F. Hutter, “Decoupled weight decay regularization,” in *International Conference on Learning Representations (ICLR)*, 2019.
- [43] M. Heusel, H. Ramsauer, T. Unterthiner, B. Nessler, and S. Hochreiter, “Gans trained by a two time-scale update rule converge to a local nash equilibrium,” *Advances in Neural Information Processing Systems (NIPS)*, vol. 30, 2017.

A Supplemental Material

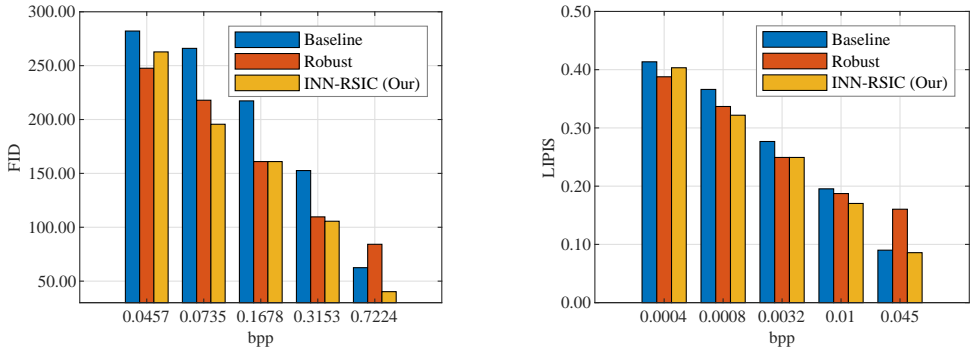
In this supplementary material, Section A.1 evaluates the robustness of our INN-RSIC initially. Next, in Section A.2, we analyze the limitations of INN-RSIC and propose a research direction to further improve the texture details of decoded RS images. Subsequently, in Section A.3, we visualize the effectiveness of QM and CGM within our INN-RSIC. Finally, Section A.4 presents the model complexity.

A.1 Robustness evaluation

The robustness of a model plays a critical role in practical deployment. Here, we employ two INN-RSIC models trained at two values of λ to enhance the decoded images of ELIC across various compression ratios. The proposed INN-RSIC trained at $\lambda = 8 \times 10^{-4}$ is used to enhance the images compressed and decoded using ELIC at different λ for the images in the testing set of DOTA, where $\lambda \in \{4, 8, 32, 100, 450\} \times 10^{-4}$. FID and LIPIS comparison results are depicted in Figure 6 (a). Comparing the FID values between the baseline and robust cases, it is observed that except for $\lambda = 450 \times 10^{-4}$, the proposed model trained at $\lambda = 8 \times 10^{-4}$ can still improve the perception quality of others.



(a) Robust performance trained at low-bitrate distortion



(b) Robust performance trained at high-bitrate distortion

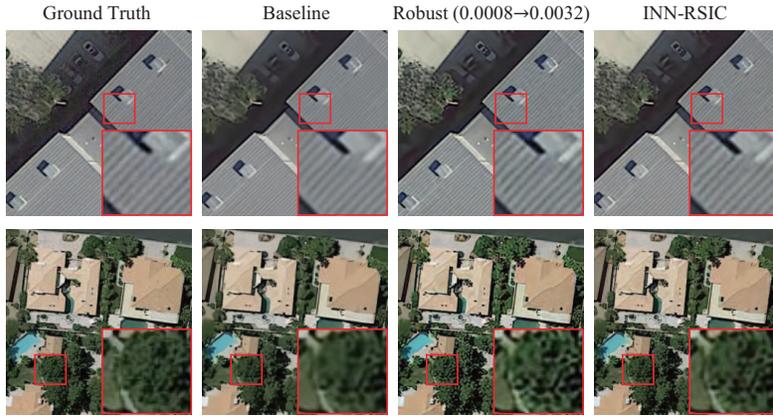
Figure 6: FID and LIPIS comparison of the baseline, robust, and our INN-RSIC. The baseline refers to testing on the decoded images of ELIC without additional improvement. The robust case indicates that our INN-RSIC trained at bpp 0.0735 (a) or bpp 0.1678 (b) is adopted to enhance the decoded images at a wide range of bpp.

Besides, our INN-RSIC trained with the corresponding λ demonstrates the most significant improvement in perception quality in terms of FID and LIPIS, except for $\lambda = 4 \times 10^{-4}$. The poorer performance of our INN-RSIC at low bpp 0.0457 (i.e., $\lambda = 4 \times 10^{-4}$) may be because the quality of the corresponding decoded image is poor at very low bpp, whereas the Gaussian distributed variables are conditioned on the decoded image. That is, the decoded image has limited guidance to recover stable results.

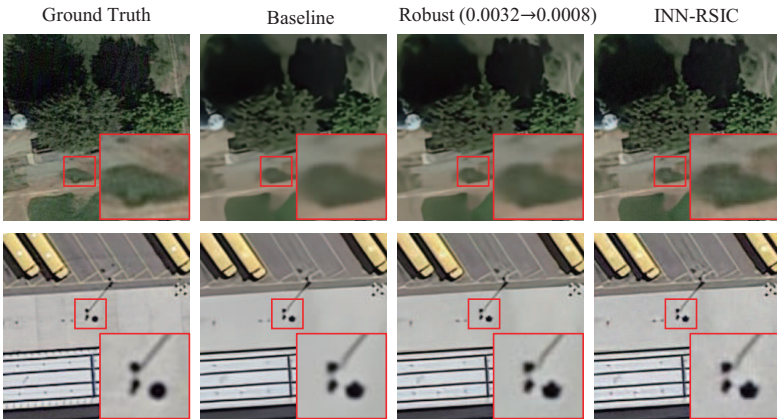
Furthermore, we investigate the robustness of our INN-RSIC model trained at high bitrate conditions in improving decoded images across different bitrate levels. The proposed INN-RSIC trained at $\lambda = 32 \times 10^{-4}$ is used to enhance the images compressed and decoded using ELIC at different λ for the images in the testing set of DOTA, where $\lambda \in \{4, 8, 32, 100, 450\} \times 10^{-4}$. FID and LIPIS comparison results are illustrated in Figure 6 (b). Comparing the FID values between the baseline and robust cases, it is observed that except for $\lambda = 450 \times 10^{-4}$, the proposed model trained at $\lambda = 32 \times 10^{-4}$ can still improve perception quality across different bitrate levels. Moreover, our INN-RSIC trained with the corresponding λ demonstrates the most significant improvement in perception quality in terms of FID and LIPIS, except for $\lambda = 4 \times 10^{-4}$.

To visualize the robust performance of the model, the robust case in Figures 7 (a) and (b) shows the enhanced images obtained by augmenting the decoded images of ELIC at high and low bitrates using the INN-RSIC model trained at low and high bitrates, respectively. The baseline denotes the image decoded by ELIC. From the results, it can be seen that although the decoded image of the robust case presents more artifacts and burrs compared to the ground truth and our INN-RSIC, it presents better visual characteristics and recovers more texture information compared to the baseline on the global vision.

In summary, the results indicate that both the proposed models trained at low and high bitrates exhibit effective enhancement of perception quality for decoded images across a wide range of bpp levels, highlighting the impressive robustness of our INN-RSIC in enhancing decoded images.



(a) The testing images "P0195" and "P0059"



(b) The testing images "P0015" and "P0089"

Figure 7: Robust performance comparison on the testing images of DOTA. (a) Low-bitrate ($\lambda = 8 \times 10^{-4}$) trained model to enhance the decoded images at high bitrate ($\lambda = 32 \times 10^{-4}$); (b) High-bitrate trained model ($\lambda = 32 \times 10^{-4}$) to enhance the decoded images at low bitrate ($\lambda = 8 \times 10^{-4}$).

A.2 Limitations

During training, we utilize decoded images as labels to guide the forward training of INN-RSIC in generating synthetic images, which are then fed into the inverse network along with Gaussian-distributed latent variables for image reconstruction. However, in the inference stage, as the ground truth cannot be obtained to feed into the forward network at the decoding end, i.e., the synthetic image cannot be derived, we resort to using labeled images instead of synthetic ones. In other words, the decoded images are fed into the inverse network along with Gaussian-distributed latent variables for enhancing the texture of the decoded images. While the texture information of the enhanced images is enriched with the assistance of Gaussian-distributed latent variables, the strictly invertible characteristic of INN inevitably affects the reconstruction quality of the enhanced image when using decoded images instead of synthetic ones.

This investigation primarily focuses on exploring the input sensitivity of our INN-RSIC model. Figure 8 showcases the images restored by INN-RSIC with synthetic images and decoded images as inputs during the inference stage. The results reveal that when synthetic images are used as input, the reconstructed image effectively recovers texture-rich details. However, when decoded images are employed as input, although some details are still recovered in the enhanced image, noticeable detail distortions emerge, particularly in texture-rich regions. To explore this issue further, we analyze the residual image between the synthetic image and the decoded image. It becomes evident that the differences contradict the invertible characteristic of INN, thereby inevitably limiting the performance of the final texture recovery.

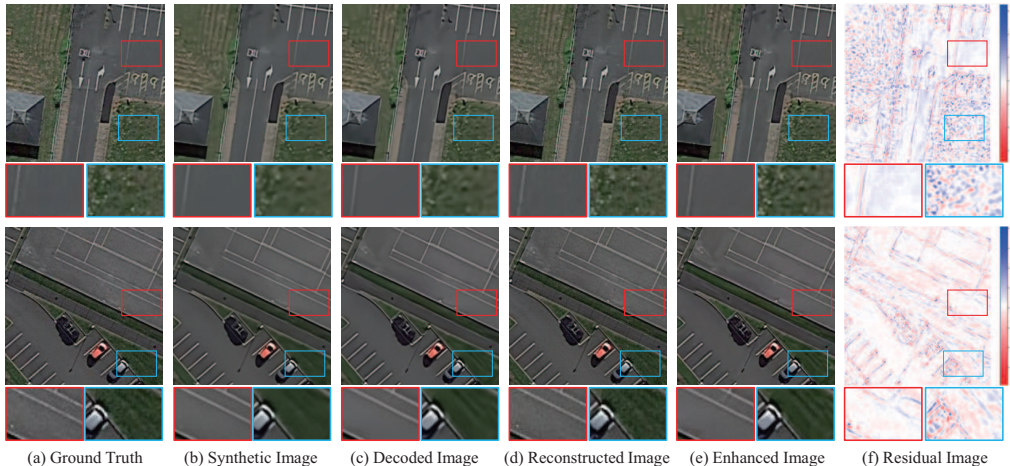


Figure 8: Visualization of images generated by our INN-RSIC with different inputs during the inference stage under $\lambda = 32 \times 10^{-4}$. The reconstructed images are obtained using the synthetic images as input, while the enhanced images are derived using the decoded images as input. The residual images illustrate the difference between the synthetic images and the decoded images.

In summary, the similarity between decoded and synthetic images significantly influences the recovery of texture-rich image details. Optimizing the algorithm design to ensure that the resulting synthetic and decoded images are as similar as possible will greatly enhance the decoding of detailed texture-rich RS images without requiring additional bitrates. This optimization holds the potential to improve the overall performance and fidelity of the INN-RSIC model, allowing for more accurate reconstruction of RS image.

A.3 QM and CGM evaluation

To visualize the effectiveness of QM and CGM, Figure 9 shows the enhanced images of our INN-RSIC with and without QM or CGM on the decoded images "P0088" and "P0097" by ELIC. The results show that although the enhanced images have higher perceptual quality than the decoded images when either QM or CGM is not available, our INN-RSIC provides the best perceptual quality when QM and CGM are used.

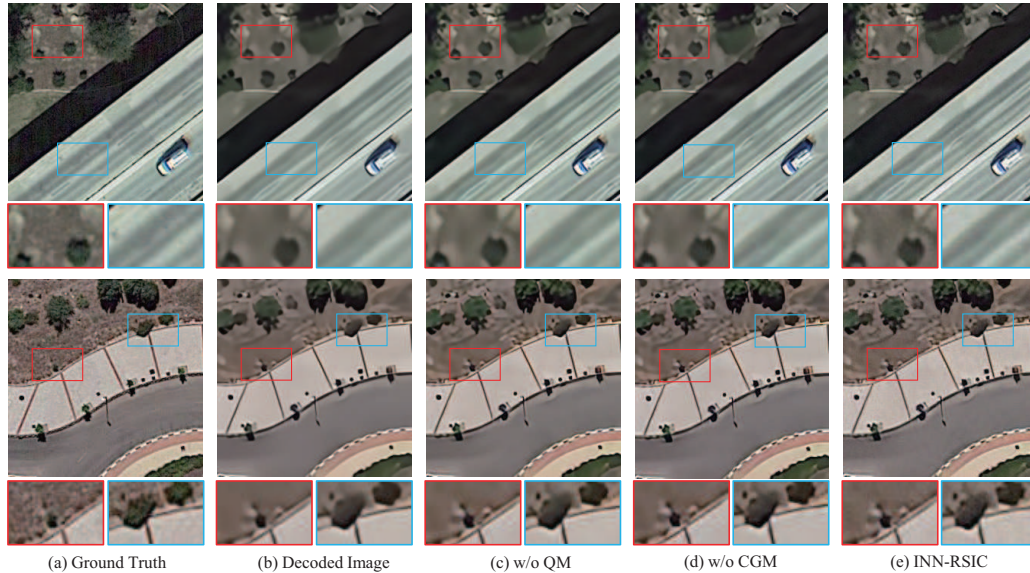


Figure 9: Visualization of the enhanced images generated by our INN-RSIC with and without (w/o) QM or CGM on the testing images "P0088" and "P0097" of DOTA. ELIC is adopted to derive the decoded images, which serve as input for our INN-RSIC for enhancement.

A.4 Model complexity

In this section, we evaluate the computational complexity of various image compression algorithms. Experiments are conducted on an Intel Silver 4214R CPU at 2.40GHz and a NVIDIA GeForce RTX 3090 Ti GPU using the PyTorch 2.0.1 framework with CUDA 11.7. The testing set of DOTA is utilized for the experiment. Table 2 presents the average results of the model complexity. From the results, it is evident that our INN-RSIC increases only 1.25M parameters, which accounts for just 2.30% of its baseline ELIC. This highlights its impressive characteristics in terms of memory storage. Additionally, concerning the decoding times of our INN-RSIC, it is observed to exhibit lower efficiency on the CPU. However, when utilizing a GPU, it demonstrates effective performance.

Table 2: Complexity comparison of several image compression algorithms. The "*" in "+*" denotes the increased complexity of INN-RSIC compared to its baseline, ELIC.

Methods	Parameters (M)	FLOPs (G)	CPU		GPU	
			Encoding Times (S)	Decoding Times (S)	Encoding Times (S)	Decoding Times (S)
Entroformer	12.67	44.76	1.3482	0.5018	0.2762	0.0919
STF	33.35	99.83	1.1395	1.3175	0.1343	0.1879
ELIC	54.46	31.66	0.7329	0.8454	0.0402	0.0224
INN-RSIC (+*)	+1.25	+31.91	/	+0.4820	/	+0.0222